more cratering events. It is perhaps significant that morphologically similar smooth, flat-floored areas of presumably ponded materials are seen in some other (noncrater) depressions on Eros (Fig. 2). Evidently there is an effective process on Eros that separates fine-grained materials from coarser regolith. Either this same process or another mechanism is able to transport the fine-grained materials over considerable lateral distances (*16*).

Some linear features, mostly grooves, previously identified in lower resolution images, can be found in the high-resolution LAF coverage as elongated depressions some tens of meters in width (Fig. 6). They are subtle depressions up to 25 m in depth (measured from shadows) with varying widths and amounts of asymmetry in profiles. Many have v-shaped cross sections indicative of the collapse of loose materials. Although some have superposed craters, indicating considerable age, other sections have sharp slope intersections and well-defined crests that may be younger. As with grooves on other bodies (*17*), their ultimate origin may be related to fractures in a more solid interior, but their surface expressions are controlled by the properties of loose materials, which may have been disturbed and in effect partially refreshed, multiple times while some other crater-induced degradation has occurred.

The LAF images provide evidence that Eros has a widespread regolith, typically several tens of meters in thickness. Exceptions may occur, especially locally on steep slopes (*18*). Similar indications of thick regoliths on small bodies have been deduced from spacecraft investigations of the tiny moons of Mars, Phobos and Deimos (*5*), and of asteroids 243 Ida (*19*) and 253 Mathilde (*20*).

References and Notes

1. For general characteristics of Eros, see J. Veverka *et al.*, *Science* **289**, 1993 (2000).
2. "Regolith" is used here in the general sense of unconsolidated fragmental material, regardless of formation or transport mechanisms.
3. The NEAR camera, the MSI, covers the spectral range from 400 to 1000 nm and has a 2.25°-by-2.90° field of view. The 244-by-537–pixel Thomson charge-coupled device has rectangular pixels that subtend 9.5 m by 16.1 m at 100 km. For details, see S. E. Hawkins *et al.*, *Space Sci. Rev.* **82**, 31 (1997) and J. Veverka *et al.*, *J. Geophys. Res.* **102**, 23709 (1997).
4. The solar incidence angle was 59° and the viewing (or emission) angle was 39°.
5. For Phobos, see P. C. Thomas *et al.*, *J. Geophys. Res.* **105**, 15,091 (2000). For the moon, see P. H. Schultz, *Moon Morphology* (Univ. of Texas Press, Austin, TX, 1976). Deimos, the outer satellite of Mars, was viewed by Viking at a resolution of 3 to 4 m [see P. C. Thomas, J. Veverka, *Icarus* **42**, 234 (1980)].
6. S. Murchie *et al.*, *Icarus*, in press.
7. For detailed passbands of filters and for reduction procedures used in analyzing MSI color data, see S. Murchie *et al.*, *Icarus* **140**, 66 (1999).
8. This calculation was done using the scaling given by P. Lee *et al.*, *Icarus* **120**, 87 (1996). If L is the size in meters of the largest block produced during the excavation of a crater of diameter D (in meters), then $L \sim 0.25\ D^{0.7}$. The largest blocks in the LAF area are about 60 to 70 m across, corresponding to a crater 3 km in diameter or larger (that is, the size of Selene or bigger).
9. For a good discussion of various possible erosional and degradational processes on airless bodies, see J. F. Lindsay, *Lunar Stratigraphy and Sedimentology* (Elsevier Scientific, New York, 1976).
10. W. L. Quaide, V. R. Oberbeck, *J. Geophys. Res.* **73** 5247 (1968).
11. Mars crossers such as Eros are in unstable orbits and must have spent most of the time since their formation in the main asteroid belt where collisions could have been relatively frequent during the earliest epochs [see P. Michel *et al.*, *Astron. J.* **116**, 2023 (1998)].
12. R. J. Pike, in *Impact and Explosion Cratering*, D. J. Roddy, R. O. Pepin, R. B. Merill, Eds. (Pergamon, New York, 1977), p. 489–509.
13. G. B. Neukum *et al.*, *Moon* **12**, 201 (1975).
14. P. H. Schultz, D. E. Gault, *Proc. Lunar Sci. Conf.* **6**, 2862 (1975).
15. The amount of material can be estimated by assuming a crater profile somewhat reduced from a fresh crater parabolic form with a depth/diameter (d/D) ratio of 0.2 (*12*). For a crater depth of 0.15 D, a central one-third of the crater would have a maximum depth of one-ninth the rim depth, or 0.017 D. For a linear depth/radius model, the deposit thickness would be one-third of the crater depth, or 0.05 D. These end-member estimates give a maximum depth of fill in a 100-m crater of 1.7 to 5 m, and a depth of fill of less than 1 m for a 20-m crater. It cannot be argued that the observed relationship between pond depth and crater diameter is explained because larger craters are on average older (form less frequently) than smaller craters and thus have had more time to accumulate ejecta from successive impact events. In such a case, at least some of the smaller craters would be expected to have as much fill as the larger ones, something that is not observed.
16. It has been suggested that electrostatic effects can both levitate and transport fine dust on airless bodies such as asteroids and the moon [see P. Lee, *Icarus*, **124**, 181 (1996) and T. Gold, *Mon. Not. R. Astron. Soc.* **115**, 585 (1955)].
17. J. Veverka *et al.*, *Icarus* **107**, 72 (1994); P. C. Thomas, J. Veverka, *Icarus* **40**, 394 (1979).
18. M. T. Zuber *et al.*, *Science* **289**, 2097; A. F. Cheng *et al.*, *Icarus*, in press.
19. R. Sullivan *et al.*, *Icarus* **120**, 119 (1996).
20. J. Veverka *et al.*, *Science* **285**, 562 (1999).

21. We thank the Mission Design, Mission Operations, and Spacecraft teams of the NEAR Project at the Applied Physics Laboratory of Johns Hopkins University for their dedicated and successful efforts that resulted in achieving the closest ever flyover of a solar system body by an orbiting spacecraft.

27 December 2000; accepted 7 March 2001

Laser Altimetry of Small-Scale Features on 433 Eros from NEAR-Shoemaker

Andrew F. Cheng,[1*] Olivier Barnouin-Jha,[1] Maria T. Zuber,[2,3] Joseph Veverka,[4] David E. Smith,[3] Gregory A. Neumann,[2] Mark Robinson,[5] Peter Thomas,[4] James B. Garvin,[3] Scott Murchie,[1] Clark Chapman,[6] Louise Prockter[1]

During the Near Earth Asteroid Rendezvous (NEAR)–Shoemaker's low-altitude flyover of asteroid 433 Eros, observations by the NEAR Laser Rangefinder (NLR) have helped to characterize small-scale surface features. On scales from meters to hundreds of meters, the surface has a fractal structure with roughness dominated by blocks, structural features, and walls of small craters. This fractal structure suggests that a single process, possibly impacts, dominates surface morphology on these scales.

The NEAR-Shoemaker mission (*1*) has measured the shape of asteroid 433 Eros from orbit with a laser altimeter (*2*), enabling quantitative assessments of the asteroid's surface morphology at scales of hundreds of meters to kilometers (*3*). Previous results from the NLR (*4*) suggested that Eros is a consolidated object whose shape is dominated by collisions. Clustered steep slopes, beyond expected angles of repose, are present over ~2% of the surface area (*4*). During the low-altitude flyover of Eros on 26 October 2000, simultaneous observations with the NLR and the multispectral imager (MSI) were obtained at a spatial resolution of ~1 m, which is at least three times the resolution achieved previously (*5*).

During the flyover, the NLR was operated continuously at a 2-Hz pulse repetition frequency. The NLR range precision is ~1 m, and the NLR boresight direction, which is illuminated by the laser, is close to the center of the MSI image field of view (*3, 6–8*). As the surface moves past the instrument boresight (owing to orbital motion, asteroid rotation, and spacecraft maneuvers), the laser spots trace out a track

[1]The Johns Hopkins University Applied Physics Laboratory, Laurel, MD 20723–6099, USA. [2]Department of Earth, Atmospheric, and Planetary Sciences, Massachusetts Institute of Technology, Cambridge, MA 02139, USA. [3]Earth Sciences Directorate, NASA/Goddard Space Flight Center, Greenbelt, MD 20771, USA. [4]Space Sciences Building, Cornell University, Ithaca, NY 14853, USA. [5]Department of Geological Sciences, 309 Locy Hall, Northwestern University, Evanston, IL 60208, USA. [6]Southwest Research Institute, 1050 Walnut Street, Suite 426, Boulder, CO 80302, USA.

*To whom correspondence should be addressed. E-mail: andrew.cheng@jhuapl.edu

along which the ranges and surface elevations are determined. Near the closest approach (5), successive laser spots were separated by ~3.7 m center to center, and the spot diameter was 1.5 m. The spots covered ~32% of the area within the track, so the altitude profiles were well sampled.

The surface elevations of the typical, heavily cratered region of Eros (9, 10) measured around the closest approach (Fig. 1) can be correlated with morphologic evidence for downslope motion of loose surface materials by measuring the elevation with respect to the gravitational potential [geoid (11)]. The closest approach occurred near a local maximum of elevation. The lengths of the two tracks were ~1.4 and 4 km (12). The average slopes along the tracks in the insets to Fig. 1 were 8° and 6°, which are typical values according to the area-weighted distribution of slopes on Eros (4, 13). The geopotential at 19°S, 331°E near the closest approach is $-50.33\ m^2\ s^{-2}$, which is intermediate between the highest and lowest values on Eros (-49.45 and $-61.47\ m^2\ s^{-2}$, respectively).

The track samples a large angular block next to a flat-bottomed crater (Fig. 2) near the local maximum in elevation. Aside from samples on top of blocks, no slopes along the track exceed expected angles of repose (4), consistent with equilibrium of an unconsolidated surface layer. The block sampled by NLR has a height of 7 m and a width of 20 m, based on six laser shots. The NLR profile may not have sampled the maximum height of the block, but it did sample a sunlit portion of it (Fig. 2C). The unsampled portion of the block did not shadow what was sampled. One laser sample was ~2 m higher than adjacent samples, suggesting that the banded appearance of this block is due to a structural facet that is being illuminated by sunlight.

The crater (Fig. 2) has a flat floor with respect to the geopotential, with a change of elevation not exceeding 2 m over a 60-m length. Similarly, flat floors in other craters in this region have been located in MSI images (9). The crater shown in Fig. 2 has a depth of 16 m versus a diameter of 190 m and is shallow in comparison with similar-sized, fresh lunar craters (14) and larger craters on Eros (9). MSI images show craters with a broad range of degradation states in this region, where subdued shallow craters are common. The MSI and NLR observations are collectively consistent with infilling of flat-floored craters as an important process. However, no evidence of infilling by downslope movement or ejecta has been identified in this region. The flatness of the region found by NLR also argues against the importance of downslope motion. Another shallow crater was transected by NLR, from distances of 625 to 684 m (Fig. 2). The depth of this crater was only 5 m for a diameter of 59 m, so its depth-to-diameter ratio is small at ~0.08, although the transect was noncentral. This crater does not have a flat floor with respect to the geopotential, but this is not surprising because the slopes (~20°) within this crater along the track are less than typical angles (28° to 36°) of repose for noncohesive materials.

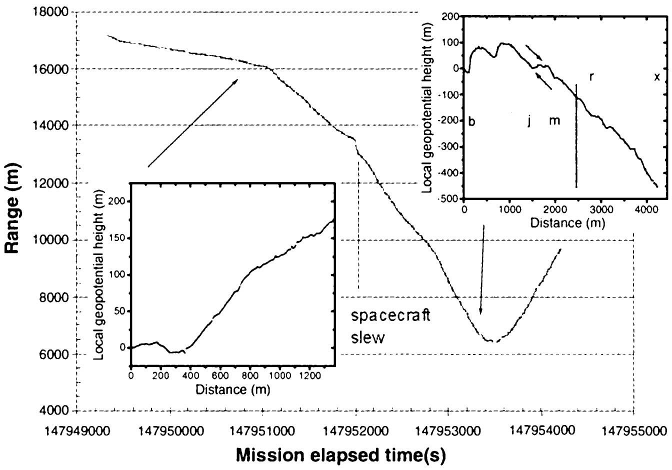

Fig. 1. Measured range to Eros surface along the NLR boresight versus MET as measured in seconds from the start of flight operations. A spacecraft slew is marked. The closest approach to surface occurred at ~147953500 s near latitude 19°S, longitude 331°E at a range of 6.4 km to the surface. The earlier interval (MET of 147950878 to 147951358 s) (lower left inset) shows geopotential height versus distance along track in meters for the earlier of two intervals discussed, with the start time indicated by an arrow on the range profile. The inset at the upper right (MET of 147953353 to 147953988 s) shows the same for the later interval, except that times of images are marked with vertical lines labeled b through x, and the step from one linear trend to another between j and m is indicated by two small arrows. In the insets, geopotential height is given by the geopotential divided by the local average effective gravity, an excellent approximation to height above the geoid for short tracks. An arbitrary reference height is used.

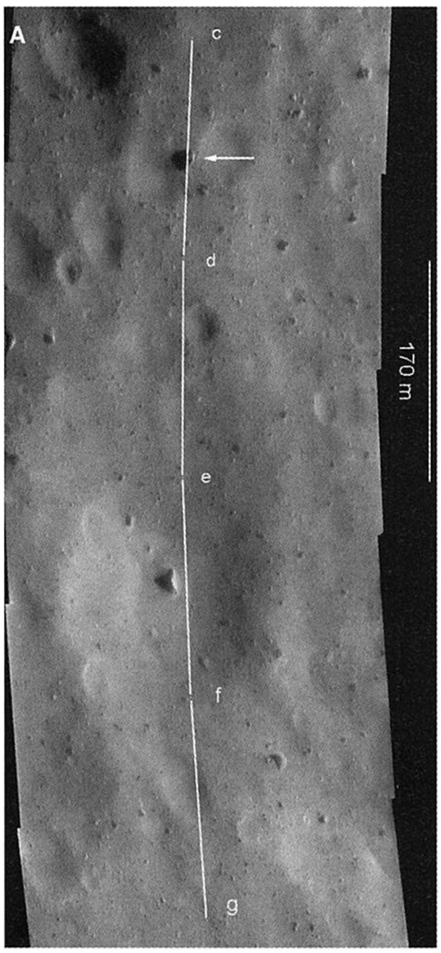

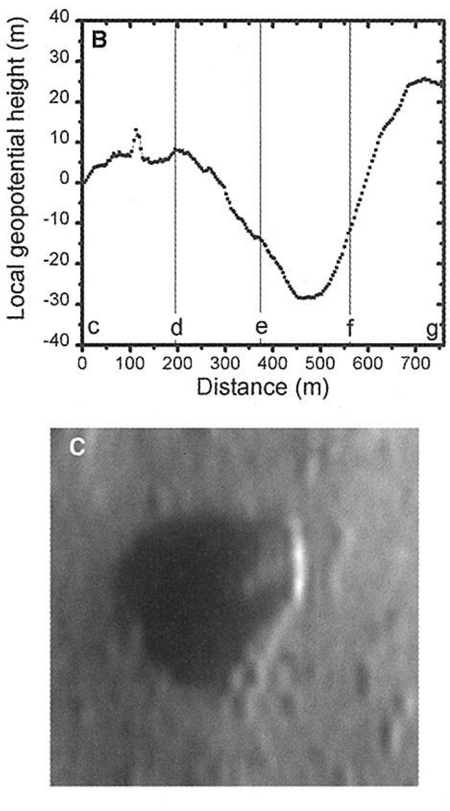

Fig. 2. Block and flat-bottomed crater. (**A**) Images at MET 147953403 to 147953503 s taken at points c through g on the NLR track; scale bar is at the right. (**B**) Elevation versus distance, with points c through g marked. (**C**) Expanded view of the block [white arrow in (A)] detected by the NLR. Numerous small positive relief features appear elongated and roughly aligned with the large block. The sun is to the right in (A) and (C) (compare shadows of the boulders).

The 26-m block to the left of the track near the center of the flat-bottomed crater is difficult to understand. This block is not the projectile that formed the crater (*15*). Blocks of this size may represent impact ejecta from craters on Eros (*9*), but if the flat-floored crater formed first and then the block fell in, a secondary crater of several times the block diameter would have formed (*15*). No such crater is seen, whereas other craters of similar size are detected in the region, but subsequent degradation may have occurred. This block and that shown in Fig. 2C have facets oriented roughly upright and parallel to a sinuous ridge and groove system to the right of the track in Fig. 2A. Moreover, numerous positive relief features in Fig. 2C appear elongated and in a similar orientation, as if controlled by planes of weakness in a competent substrate.

Structural features and/or crater rims are associated with the step from one linear trend to another in the upper right inset to Fig. 1, according to MSI images (*9*), which reveal that the elevation peaks at approximate distances of 1900 and 1700 m are ridge crests. The depression at a distance of 2000 m is a shallow crater. Topography of up to a few tens of meters is associated with these features. A relatively boulder-rich area farther down the slope shows two elevation features, at approximate distances of 3750 and 3900 m, which are subtle ridges associated with ~10 m of relief.

The contributions to surface roughness from structural features at various scales and from blocks can be quantified by the root mean square (rms) height $\sigma = \langle [h(x) - h(x + L)]^2 \rangle^{0.5}$ calculated from NLR profiles, where $h(x)$ is the linearly detrended geopotential height and height differences are evaluated at all pairs of points separated by a baseline L. Many surfaces are almost self-affine (*16*) over two or more decades of L, meaning that a power-law behavior $\sigma = \sigma_0(L/L_0)^H$ applies, a normalizing constant σ_0, $L_0 = 1$ m, and the Hurst exponent H. For a rough terrestrial a'a lava flow up to meter scale (*17*), $\sigma_0 = 0.15$ m and $H = 0.58$.

One track (Fig. 1, lower left inset) is analyzed as a whole and as two separate segments, with distances of <500 and >500 m. From MSI images (*9*), the shorter segment samples a broad trough, and the longer segment samples a ridge crest. The whole track has an almost self-affine structure over scales from a few meters to a few hundred meters and is rougher than the a'a lava (*17*) if extrapolated to a 1-m baseline. The turndown of the rms height at large baselines occurs at 250 m for the whole track and for the longer crest segment and at 128 m for the shorter trough segment. This behavior reflects the size of the largest structural features sampled as well as the influence of track length when detrended profiles are analyzed. Comparison of the trough segment with the crest segment in the self-affine regime below 128 m shows that the crest is slightly rougher than the trough.

Another track (Fig. 1, upper right inset) is analyzed in two segments: (i) segment a to l, with the flat-bottomed crater and the small ridges, and (ii) segment m to x, with high block densities, according to MSI images (*9*). In addition to rms height, which is marked with symbols, Fig. 3B gives the 75 and 25% quartiles of the height difference distributions at each baseline. The rms heights are almost equal to the 75% quartile values. The quartile curves parallel the rms height curves, further supporting the self-affine structure of the surface and the difference between the Hurst exponents of the two segments. The block-rich m to x segment is slightly smoother at the smallest baselines but is much smoother at 100-m scales than the a to l segment with its structural features. Hence the two segments of Fig. 3B are similar in roughness at scales of a few meters, presumably because of the similar distributions of small blocks, whereas the a to l segment is more rugged at scales of 100 m and larger because of its structural features. The quartile statistics of the track in Fig. 3A are similar to those of Fig. 3B.

The NLR profile in the upper right inset to Fig. 1 further suggests that the ridge crests are rougher than the troughs. This is quantified by rms height differences at 8-m baselines in two cases: near ridge crests and away from them (*18*). Roughness measured by rms height was 2.1 m near the ridge crests but only 0.7 m away from them. MSI images of this region show a profusion of blocks (*9*), and the greater roughness of the ridge crests may result from higher block densities on ridge crests when compared with troughs.

The NLR observed a typical region on Eros at high spatial resolution, but phenomena such as greater roughness near ridge crests may not generalize to other regions or to scales much larger than 100 m. Evidence is found for filling in of craters to a few tens of meters (*19*). Most of these craters were accumulated over $>10^9$ years while Eros was still within the main asteroid belt (*9*, *20*). This age would imply an average rate of infilling of craters, or resurfacing, estimated as 10^{-8} m year^{-1}.

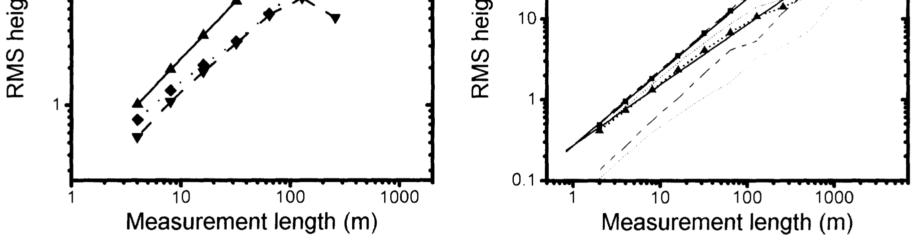

Fig. 3. (**A**) Fractal analysis of the entire track in the lower left inset to Fig. 1 is shown by the solid line with triangles; analysis of distances <500 m (within trough) is shown by the dashed line with triangles; and analysis of distances >500 m (wall and crest of ridge) is shown by the dotted line with diamonds. (**B**) Analyses of the track in the upper right inset to Fig. 1. MET of 147953353 to 147953647 s (points a through l) is shown by the dashed line with squares, and the 25 and 75% quartiles are shown by dashed lines. MET of 147953647 to 147953980 s (points m through x) is shown by the dotted line with triangles, and the 25 and 75% quartiles are shown by dotted lines.

References and Notes

1. A. F. Cheng *et al.*, *J. Geophys. Res.* **102**, 23695 (1997).
2. T. D. Cole *et al.*, *Space Sci. Rev.* **82**, 217 (1997); A. F. Cheng *et al.*, *Icarus* **148**, 572 (2000). The NLR is a direct-detection laser altimeter with a Cr:Nd:yttrium-aluminum-garnet transmitter.
3. M. T. Zuber, D. E. Smith, A. F. Cheng, T. Cole, *J. Geophys. Res.* **102**, 23761 (1997).
4. M. T. Zuber *et al.*, *Science* **289**, 2097 (2000). The interior of Eros is almost homogeneous and has an average density of 2670 kg m^{-3}. There is a small center-of-figure offset from the center of mass that is consistent with the presence of an unconsolidated regolith layer of up to 100 m in thickness.
5. The closest approach distance to the surface was 5.3 km, but at that time, the closest point on the surface was on the night side of the asteroid and could not be imaged. The observations were targeted to the day side, and the closest range to the observation point was 6.4 km. Before the flyover, the closest orbit was a 35-km-radius (from the asteroid center of mass), circular polar orbit. The maximum equatorial radius of Eros (*4*) is 17.5 km. From mission elapsed time (MET) 147953400 to 147953600 s, the average distance between successive spots was 3.7 m. The NLR beamwidth (*3*) is 235 μrad, so the spot diameter was ~1.5 m during that interval.
6. The direction of the NLR boresight relative to the MSI field of view was determined by a comparison of the NLR range data with simultaneous images (*7*). Instances when the laser boresight slewed off and on the limb of the asteroid are readily identified as gaps in the laser data and are correlated with images of the Eros limb to yield constraints on the relative alignments of the MSI and NLR. Laser returns are detected consistently whenever the boresight is on the asteroid. During 26 October 2000, from MET 147930567.25 to 147999674.5 s, the NLR detected returns from 52,123 consecutive laser shots, with zero noise returns and zero missed returns during this sequence. The small data gap shown in Fig. 1 is caused by high-level processing, which rejects a small fraction of valid range returns that cannot be located

accurately in Eros latitude and longitude (*4*). Several cases have been found where the laser illuminated a boulder at almost the same time as when an image was obtained, yielding a feature in the NLR profile and an almost simultaneous image in which the boulder can be identified. These cases yield NLR boresight determinations to within an ~2-pixel uncertainty within the image frame (*7*). During the low-altitude flyover, the NLR boresight was located at line = 220, sample = 255, in the rectified MSI pixel format (*8*), where the full frame has 412 lines and 537 samples and where each pixel is square and subtends 95.9 μrad. Once the boresight alignment of the NLR is determined in relation to the MSI, each of these coordinated data sets enhances the interpretation of the other. The MSI helps to characterize topographic features detected by the NLR, e.g., by distinguishing between grooves and craters. The NLR helps to distinguish brightness variations caused by topography from those caused by differences in reflectivity.

7. A. F. Cheng *et al.*, *Icarus* **148**, 572 (2000).
8. S. Murchie *et al.*, *Icarus* **140**, 66 (1999).
9. J. Veverka *et al.*, *Science* **292**, 484 (2001); J. Veverka *et al.*, *Science* **289**, 2088 (2000).
10. Locations on the asteroid surface are specified in a planetocentric system referenced to the center of mass (*4*). The closest approach observations could not be targeted to any specific surface feature because of navigational uncertainty.
11. Elevation is determined in relation to the potential arising from the mass of the asteroid and the centrifugal potential, or geopotential, given by

$$\Phi(\mathbf{x}) = -\int d^3\mathbf{x}' \frac{G\rho}{|\mathbf{x}-\mathbf{x}'|} - \frac{\Omega^2 r^2}{2}$$

where the gravitational potential at **x** is found from an integral over the volume of the asteroid, r is the distance from the point **x** to the rotation axis, and Ω is the rotation rate 3.31166×10^{-4} rad s^{-1} (*4, 7*). The geopotential is determined by numerical integration over the volume of Eros assuming a constant density (*4*). The geopotential height h measured in meters is defined by (*21*)

$$h(\mathbf{x}_i) = |\Phi(\mathbf{x}_i)/g_{\mathrm{avg}}|$$

Hence $h(x)$ is proportional to geopotential but is scaled by a factor g_{avg}, the local average magnitude of the effective gravitational acceleration over a short track, typically <1 km in length. The later track in Fig. 1 was analyzed in six segments that were concatenated.
12. Distance is defined with the line that is the least squares best fit to a short track of laser spots in three dimensions. The position of each laser spot is projected onto this line, and distance is measured along the line. Distance is determined independently for each of the six segments concatenated to form the later track in Fig. 1 (upper right inset). The slope between two samples is not determined with this projected distance; slope is determined from the geopotential height difference and the magnitude of the displacement vector. Hence the slope is not simply related to the graphical slopes of the curves in the insets to Fig. 1.
13. The area-weighted slope distribution refers to slopes in three dimensions and, specifically, the angle α between the local effective gravity and the inward surface normal. The NLR measures slopes along a track that can be approximated as linear for a short distance. If the track is oriented randomly within the local tangent plane to the surface, then the slope along the track α_T (the angle between the track and the local horizontal plane, perpendicular to the local gravity) is related statistically to the slope in three dimensions. Specifically, the two slopes are related on the average by $\langle \sin \alpha_T / \sin \alpha \rangle = 2/\pi$.
14. The depths of small fresh lunar craters are ~0.2 times the diameters [H. Melosh, *Impact Cratering: A Geologic Process* (Oxford Univ. Press, New York, 1989)].
15. Crater scaling relations (*22*) indicate that a 14-m block, which would have the same cross-sectional area as the block in the flat-floored crater, would have created a crater of 190 m in diameter (assuming gravity scaling), given an impact velocity of 240 m s^{-1}. In such an impact, the projectile would be buried below the surface (*23*). On the other hand, if the block was ejected from an impact elsewhere on Eros, it impacted the surface below the escape velocity of 3 to 17 m s^{-1} (*24*) and would not necessarily fracture. At an impact velocity of 10 m s^{-1}, a crater of 64 m in diameter would be created.
16. D. Turcotte, *Fractals and Chaos in Geology and Geophysics* (Cambridge Univ. Press, New York, 1997). The fractal dimension D is related to the Hurst exponent H by $D = 2 - H$.
17. M. Shepard, B. Campbell, *Icarus* **134**, 279 (1998). The roughness of the terrestrial a'a lava cannot be extrapolated to scales >1 m in a fractal manner, because of the effect of competing physical processes in determining texture. It remains to be established whether roughness on Eros behaves fractally on scales as short as 1 m.
18. On-ridge intervals are as follows: 147953865 to 147953871 s, 147953884 to 147953889 s, 147953898 to 147953910 s, and 147953929 to 147953936 s. Off-ridge intervals are as follows: 147953871 to 147953877 s, 147953890 to 147953897 s, 147953911 to 147953929 s, and 147953936 to 147953941 s.
19. The depth of infill can be inferred by assuming that the depth of a fresh crater is 0.2 times the diameter. This argument gives ~20 m of infill for the flat-floored crater of Fig. 2. An alternative interpretation is that the flat bottom of the crater between points e and f is caused by the failure of the cratering event to excavate into a flat competent substrate (*25*). Laboratory impact experiments into a layered target, with an unconsolidated layer on top of a hard competent substrate, show that flat-bottomed craters form when the crater diameter is 8 to 10 times the depth of the unconsolidated layer, which would be 17 m deep in this interpretation. However, the crater morphology is more suggestive of mantling (*9*). A complication is that the flat-bottomed crater is situated within a larger depression that extends roughly from point d to a distance of 550 m in Fig. 2B, beyond point f. This larger depression is 370 m across along the track, but only 40 m deep. The flat-bottomed crater and the larger depression around it may comprise a single impact crater, in which case the apparent rim at the level of points e and f could result from variation in the mechanical properties of the regolith with depth. Available evidence does not resolve this issue, but in any case, inferred regolith depths would be tens of meters, consistent with previous work (*4, 7, 9*). The original depth of a fresh 370-m crater would be ~74 m, and the flat crater floor could result from 34 m of infill or (less likely) from the presence of a hard competent substrate 40 m below the original surface.
20. Eros is currently in a chaotic orbit, which evolves on million-year time scales and which crosses the orbit of Mars and approaches that of Earth (*26*). The flux of impactors on Eros in its present orbit was calculated by a Monte Carlo method (*27*) with a projectile distribution in orbital elements as observed for minor planets, but a size distribution extrapolated downward to values relevant to cratering on asteroids [e.g., (*28*)]. In its present orbit, Eros would require 10^{10} years to reach equilibrium densities of craters >200 m (*27*), implying that most of the larger craters formed while Eros was still within the main belt (*9*).
21. P. Thomas *et al.*, *Icarus* **107**, 23 (1994); P. Thomas *et al.*, *Icarus* **120**, 20 (1996).
22. K. Holsapple, *Annu. Rev. Earth Planet. Sci.* **21**, 333 (1993).
23. W. K. Hartmann, *Icarus* **63**, 69 (1985).
24. D. K. Yeomans *et al.*, *Science* **289**, 2085 (2000).
25. W. Quaide, V. Overbeck, *J. Geophys. Res.* **73**, 5247 (1968).
26. P. Michel, P. Farinella, C. Froeschle, *Astron. J.* **16**, 2023 (1998).
27. O. Barnouin-Jha, A. Cheng, *Lunar Planet. Sci.* **XXXI** (abstr. 1255) (2000) [CD-ROM].
28. R. Greenberg *et al.*, *Icarus* **120**, 106 (1996).
29. The NLR and MSI investigations are supported by NASA under the NEAR-Shoemaker Project. We acknowledge the contributions of the spacecraft and mission operations teams.

15 December 2000; accepted 7 March 2001

Matriarchs As Repositories of Social Knowledge in African Elephants

Karen McComb,[1,2]* Cynthia Moss,[2] Sarah M. Durant,[3] Lucy Baker,[1,2] Soila Sayialel[2]

Despite widespread interest in the evolution of social intelligence, little is known about how wild animals acquire and store information about social companions or whether individuals possessing enhanced social knowledge derive biological fitness benefits. Using playback experiments on African elephants (*Loxodonta africana*), we demonstrated that the possession of enhanced discriminatory abilities by the oldest individual in a group can influence the social knowledge of the group as a whole. These superior abilities for social discrimination may result in higher per capita reproductive success for female groups led by older individuals. Our findings imply that the removal of older, more experienced individuals, which are often targets for hunters because of their large size, could have serious consequences for endangered populations of advanced social mammals such as elephants and whales.

Although there is considerable interest in the evolution of social intelligence (*1–4*), we still know little about how wild animals gain and store information about social companions or whether the possession of superior social knowledge enhances fitness. When mammals live in complex fission-fusion societies (*5–7*), individuals may encounter hundreds of others during their daily ranging patterns, and time intervals between repeated exposures to the same individuals may be extremely long. Under these circumstances, the problem of distin-